Inorganic Chemistry

pubs.acs.org/IC

Article

Enhanced Photoluminescence and Reduced Dimensionality via Vacancy Ordering in a 10H Halide Perovskite

Hang Liu, Hassan Hafeez, David B. Cordes, Alexandra M. Z. Slawin, Gavin Peters, Stephen L. Lee, Ifor D. W. Samuel, and Finlay D. Morrison*

Cite This: https://doi.org/10.1021/acs.inorgchem.2c04433

Read Online

ACCESS | Metrics & More | Article Recommendations | Supporting Information

ABSTRACT: Vacancy-ordered halide perovskites have received great interest in optoelectronic applications. In this work, we report the novel inorganic halide $Cs_{10}MnSb_6Cl_{30}$ with a distinctive 10H (10-layer hexagonal) perovskite polytype structure with $(hcccc)_2$ stacking. $Cs_{10}MnSb_6Cl_{30}$ has 30% B-site vacancies ordered at both corner- and face-sharing sites, resulting in $[MnSb_6Cl_{30}]^{10-}{}_n$ columns, i.e., a reduction of octahedral connectivity to 1D. This results in enhanced photoluminescence in comparison to the previously reported 25% vacancy-ordered 3C polytype $Cs_4MnSb_2Cl_{12}$ with 2D connectivity. This demonstrates not only the existence of the 10H perovskite structure in halides but also demonstrates the degree of B-site deficiency and stacking sequence variation as a direction to tune the optical properties of perovskite polytypes via vacancy rearrangements.

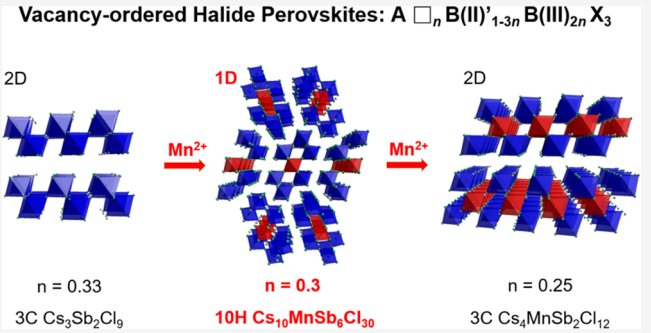

INTRODUCTION

In the past decade, both inorganic and organic−inorganic hybrid halide perovskites have generated immense research interest for application in optoelectronic, photocatalytic, and light-emitting diode devices because of their favorable electronic structure, structural tunability, and low cost of fabrication.[1] For the stoichiometric perovskite with the formula ABX_3, the B-site cation occupies one quarter of the interlayer octahedral voids formed by the close-packed AX_3 layers. Several perovskite polytypes exist depending on the close packing sequence, which can be cubic (ABC, e.g., in the prototypical perovskite mineral $CaTiO_3$[2] or the halide $CsPbCl_3$[3]), hexagonal (ABA, e.g., $BaNiO_3$[4] or $CsNiCl_3$[5]), or a mixture of both. The latter two cases demonstrate the hexagonal perovskite polytypes.[6]

The various perovskite polytypes can be informatively described using a combination of Jagodzinski and Ramsdell notations.[7] The Jagodzinski notation describes the repeat stacking sequence of cubic (c) and hexagonal (h) close-packed layers, whereas the Ramsdell notation takes the form *n*M where *n* describes the number of layers in the aristotype unit cell and M = C, H, or R indicating cubic, hexagonal, or rhombohedral parent symmetry, respectively. For example, a conventional perovskite formed by three cubic (ccc, i.e., ABC) packed AX_3 layers is denoted as 3C (e.g., $SrTiO_3$[8]), a perovskite with only hexagonal packing (hh, i.e., AB) is denoted as 2H (e.g., $BaNiO_3$ and $CsNiCl_3$), the hexagonal polytype with four cubic and two hexagonal AX_3 layers, $(cch)_2$, in a hexagonal primitive cell is denoted as 6H (e.g., $RbMgF_3$[9] or $BaFeO_3$[10]), and so on. To specifically define each hexagonal polytype, a combination of Ramsdell and Jagodzinski notations is unambiguous, e.g., 10H $(hhccc)_2$,[11] 10H $(hhhcc)_2$,[12] and 10H $(hcccc)_2$.[13]

A key feature of these perovskite polytypes is the connectivity of the BX_6 units, which can be either corner-sharing octahedra (CSO) formed in cubic close-packed stacking or face-sharing octahedra (FSO) generated by hexagonal close-packed stacking. For stoichiometric perovskites, CSO in 3C materials results in three-dimensional (3D) octahedral connectivity, but the 2H (hh) polytype with only FSO exhibits one-dimensional (1D) chains of octahedra. For other hexagonal polytypes, varying degrees of CSO and FSO exist while retaining a 3D network, and this variation of connectivity influences the band structure due to the different B−X orbital interactions in the FSO.[14] Increasing degrees of FSO generally leads to an increase of the band gap.[15] For inorganic perovskites, substitution of higher valence B cations is a common strategy to adjust the octahedral connectivity by the introduction of compensating B-site vacancies to maintain electroneutrality.[16] The preferred occupancy (ordering) of vacancies at specific sites disrupts the connectivity of the 3D octahedral framework, resulting in a reduction of dimension-

Received: December 19, 2022

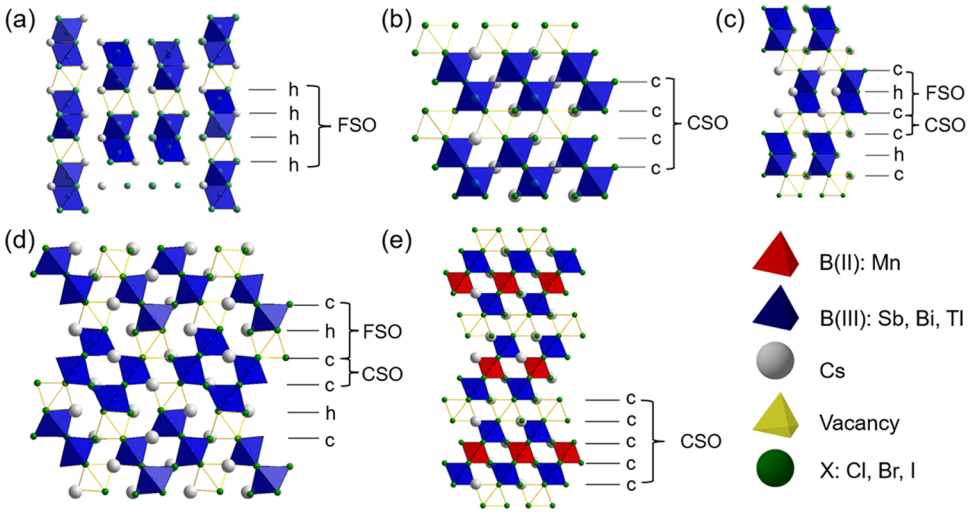

Figure 1. Polyhedral representation of the structures of $A_3B_2X_9$ B-site-deficient perovskites: (a) 0D 2H $(h)_3$ $Cs_3Tl_2Cl_9$, (b) 2D 3C $(c)_3$ $Cs_3Bi_2Br_9$, (c) 0D 6H (hcc) $Cs_3Bi_2I_9$, (d) 1D 6H $(hcc)_2$ $Cs_3Bi_2Cl_9$ type, and (e) 2D 3C $(c)_4$ $Cs_4MnSb_2Cl_{12}$. For ease of comparison, all structures are viewed along the close packing layers.

ality to 2D, 1D, or 0D, depending on the relative amount and position of the vacancies. In comparison with 3D counterparts, lower dimensional perovskites have been proven to be important materials with highly efficient light emitting performance and improved moisture stability.[17]

In the recent years, the B-site-deficient halide perovskites $A_3B(III)_2X_9$ (A = K, Rb, Cs; B = Sb, Bi, Tl, etc.; and X = Cl^-, Br^-, I^-) have been revisited to investigate the relationship between the crystal and electronic structure (specifically band gap).[18−21] It is typical for these $A_3B_2X_9$ compounds that AX_3 forms close-packed layers with the B cations occupying 2/3 of the octahedral sites with the remaining 1/3 vacant. The most well-defined $A_3B_2X_9$ structures can be classified into four aristotype structures in relation to the packing sequence of the fully occupied perovskite equivalent and the resulting vacancy ordering as shown in Figure 1. $Cs_3Tl_2Cl_9$ is derived from the 2H parent with only hexagonal $(h)_2$ stacking but with 1/3 B-site vacancies ordered in each FSO layer, resulting in the 0D connectivity of B_2X_9 "dimers," Figure 1a.[22] In comparison, $Cs_3Bi_2Br_9$ is based on conventional cubic close-packed 3C $(c)_3$ perovskites with vacancies ordered in every third CSO layer to generate a 2D layered structure, Figure 1b.[23] Both $Cs_3Bi_2I_9$ (also denoted as $Cs_3Cr_2Cl_9$ type)[24] and $Cs_3Bi_2Cl_9$[25] have 6H $(hcc)_2$ stacking, but the different vacancy ordering results in differing dimensionality of the octahedral connectivity. In $Cs_3Bi_2I_9$, the vacancies occur only in the corner-sharing octahedral (CSO) sites, resulting in a 0D dimer structure, Figure 1c, which is similar to $Cs_3Tl_2Cl_9$ but with layering of the dimers in the close packing plane.[26] In contrast, $Cs_3Bi_2Cl_9$ has vacancy ordering at the FSO sites with 50% occupancy, instead resulting in 1D connective columns of four octahedra running perpendicular to the closed-packing direction, Figure 1d. These examples neatly demonstrate the opportunity for structural tuning through vacancy ordering.

Recently, a new series of B-site-deficient perovskites with 25% vacancies was reported by Vargas et al. and can be described by the formula $A_4B'(II)B(III)_2X_{12}$ (A = Cs^+, Rb^+; B′ = Mn^{2+}, Cd^{2+}, Cu^{2+}; B = Sb^{3+}, Bi^{3+}, In^{3+}; and X = Cl^-, Br^-).[27−30] These compounds have an entirely cubic close-packed AX_3 structure (the same as $Cs_3Bi_2Br_9$, Figure 1b), but the B-site vacancies order such that every fourth CSO layer is empty rather than every third, Figure 1e. From a general view, both $A_3B_2X_9$ and $A_4B'B_2X_{12}$ belong to special cases of B-site-deficient halide perovskite with the general formula $A-(\square_nB'_{1-3n}B_{2n})X_3$ with n = 0.33 and 0.25, respectively (n represents the fraction of vacancies per perovskite formula unit). By varying n, a series of potential new compounds and structures with varying octahedral connectivity can be generated, which is dependent on the extent and configuration of vacancy distribution as well as the AX_3 packing sequence of the structure.

In this study, we report the synthesis of a novel 1D halide derivative 10H perovskite $Cs_{10}MnSb_6Cl_{30}$ (n = 0.3) with ordered vacancies at both CSO and FSO sites, which displays enhanced photoluminescence compared to the related 2D $Cs_4MnSb_2Cl_{12}$ compound. The discovery of this vacancy-ordered 10H halide demonstrates the strategy to tailor the structure and properties of B-cation-deficient perovskites through a combination of vacancy ordering and stacking sequence variation.

EXPERIMENTAL METHODS

Synthesis. Raw materials, CsCl (99%), $MnCl_2$ (97%), $SbCl_3$ (99%), $MgCl_2$ (99%), and hydrochloric acid in water (37%), were purchased from Alfa Aesar and used without further purification. All other solvents were obtained from commercial routes and used as-received.

$Cs_{10}MnSb_6Cl_{30}$ single crystals (SCs) were prepared by a hydrothermal reaction in a 40 mL stainless steel autoclave. To obtain the required high chloride ion concentration during synthesis while minimizing the amount of HCl used, an excess amount of $MgCl_2$ (10 mmol, 0.9521 g) was dissolved in 5 mL of dilute 20% HCl to obtain a transparent solution. Stoichiometric amounts of $MnCl_2$ (1 mmol, 0.1258 g) and $SbCl_3$ (6 mmol, 1.3688 g) were then dissolved in the solution. To prevent the formation of the secondary phase $Cs_3Sb_2Cl_9$, a smaller amount of CsCl (1 mmol, 0.1684 g) was finally added to the solution. The pressure vessel was then heated in an oven at 150 °C for 24 h before cooling to room temperature in air. The product was filtered by vacuum filtration, washed with ethanol several times, and dried in a vacuum desiccator overnight.

$Cs_{10}MnSb_6Cl_{30}$ powder was also prepared by solid-state synthesis. Stoichiometric amounts of CsCl (10 mmol, 1.6836 g), $MnCl_2$ (1 mmol, 0.1258 g), and $SbCl_3$ (6 mmol, 1.3688 g) were mixed and ground together in a Fritsch Pulverisette planetary ball mill at 600

https://doi.org/10.1021/acs.inorgchem.2c04433
Inorg. Chem. XXXX, XXX, XXX−XXX

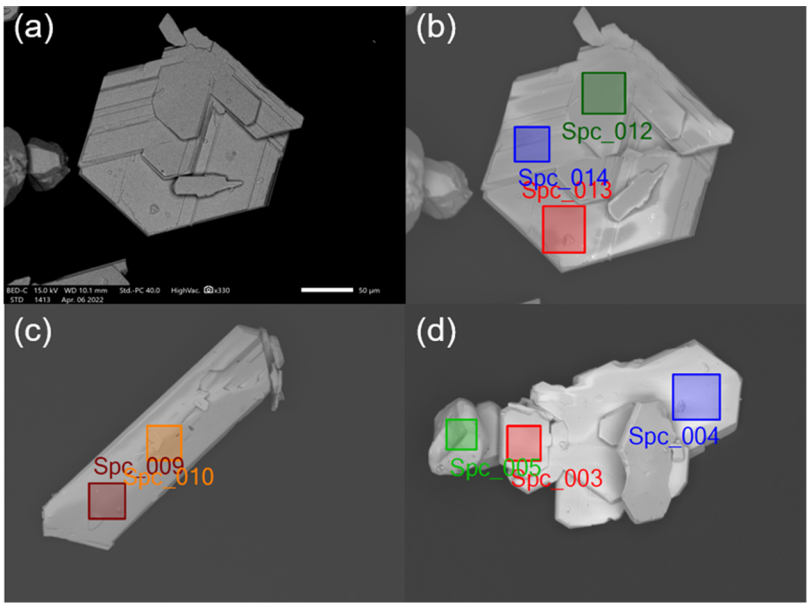

Figure 2. SEM morphologies (secondary electron image, a) and EDS analysis sites (back-scattered electron images, b–d) of $Cs_{10}MnSb_6Cl_{30}$ and secondary phase $Cs_3Sb_2Cl_9$ single crystals (far left crystal in panel (d), indicated by the Spc_005 data point). The scale bar in panel (a) is 50 μm.

Table 1. Compositional Analysis Using EDS for $Cs_{10}MnSb_6Cl_{30}$ Single Crystals, Secondary ($Cs_3Sb_2Cl_9$) Phase Crystals, and $Cs_{10}MnSb_6Cl_{30}$ Powder Prepared by Solid-State Synthesis

	Cs (atom %)	Mn (atom %)	Sb (atom %)	Cl (%)
SCs $Cs_{10}MnSb_6Cl_{30}$	21.71 ± 0.12	1.95 ± 0.06	13.90 ± 0.09	62.43 ± 0.19
secondary phase $Cs_3Sb_2Cl_9$	20.63 ± 0.3	NA	17.18 ± 0.25	62.18 ± 0.46
powder $Cs_{10}MnSb_6Cl_{30}$	22.44 ± 0.12	2.02 ± 0.06	14.04 ± 0.09	61.51 ± 0.19

rpm for 2 h using 60 cm^3 Teflon pots and high-wear-resistant zirconia media. The mixture was then uniaxially pressed into a 10 mm diameter pellet using a stainless steel pellet die under a load of 1 ton and heated at 220 °C in a furnace for 2 h.

$Cs_4MnSb_2Cl_{12}$ powder was prepared by a conventional solution route.[27] Stoichiometric amounts of $MnCl_2$ (1 mmol, 0.1258 g) and $SbCl_3$ (2 mmol, 0.4562 g) were dissolved in 3 mL of conc. 37% HCl on a hot plate at 90 °C with continuous magnetic stirring. CsCl (1 mmol, 0.1684 g) was then dissolved in 2 mL of conc. 37% HCl with stirring. $Cs_4MnSb_2Cl_{12}$ powder was obtained by adding the precursor CsCl solution dropwise to the $MnCl_2$ and $SbCl_3$ solution. The resulting powder was washed with ethanol and dried under vacuum for 12 h.

Characterization. Single crystals prepared by hydrothermal reactions and powders synthesized by either a precipitation or solid-state method were characterized by single-crystal and powder X-ray diffraction (SCXRD and PXRD), respectively. X-ray diffraction data for $Cs_{10}MnSb_6Cl_{30}$ were collected using a Rigaku FR-X Ultrahigh Brilliance Microfocus RA generator/confocal optics with an XtaLAB P200 diffractometer [Mo Kα radiation (λ = 0.71073 Å)]. Intensity data were collected using ω steps accumulating area detector images spanning at least a hemisphere of reciprocal space. Details of structural solution are provided in the Supporting Information. PXRD data were obtained using a PANalytical Empyrean diffractometer with Cu Kα1 (λ = 1.5406 Å) and 2θ angle ranging from 3 to 70° at 298 K. Basic Rietveld refinements of PXRD data using GSASII[31] were performed to confirm phase purity and for the determination of lattice parameters. The structures of all samples were refined using their corresponding structural model obtained from single-crystal data.[27]

Morphology observation and elemental analysis based on energy-dispersive X-ray spectroscopy (EDS) were performed on the single crystals to confirm the composition and stoichiometry and to exclude the presence of magnesium using a JEOL JSM-IT200 scanning electron microscope (SEM) with an accelerating voltage of 15 kV.

Pseudoabsorbances were calculated from steady-state UV–vis diffuse reflectance data recorded using a JASCO-V650 double-beam spectrophotometer based on the Kubelka–Munk transformation.[32] Tauc plots assuming both direct and indirect transitions were applied to the pseudoabsorbance spectra to estimate the band gap of $Cs_{10}MnSb_6Cl_{30}$. Powders from ground $Cs_{10}MnSb_6Cl_{30}$ SCs and solution-prepared $Cs_4MnSb_2Cl_{12}$ were used in the UV–vis diffuse reflectance measurements (see the Supporting Information for more details).

Steady-state emission and excitation spectra of the powder samples were recorded at 298 K using a spectrofluorometer (Edinburgh Instruments FLS980) with a 150 W ozone-free xenon arc lamp as the excitation source. The photoluminescence quantum yield measurement was conducted using an absolute quantum yield spectrometer model C9920-02 (Hamamatsu, Japan) equipped with a xenon light source. A quartz substrate was used to obtain the blank measurement shown in Figures S6 and S7. All PL, PLE, and PLQY measurements were performed on the solid-state synthesized $Cs_{10}MnSb_6Cl_{30}$ and solution-prepared $Cs_4MnSb_2Cl_{12}$ powders.

Dielectric measurements and thermogravimetric and differential scanning calorimetry (TG-DSC) analysis were performed to examine the thermal stability and possible phase transition in $Cs_{10}MnSb_6Cl_{30}$ (see the Supporting Information for details).

The magnetic susceptibility of ground SCs $Cs_{10}MnSb_6Cl_{30}$ was measured using a Quantum Design MPMS3 SQUID magnetometer. For magnetic measurements, single crystals were favored over solid-state powders to avoid any risk of signals from impurities picked up from the stainless-steel pellet die during synthesis; note that small $Cs_3Sb_2Cl_9$ crystals were only present in negligible amounts in the SC samples and in any case is diamagnetic. Approximately 58 mg of samples were enclosed within in a polycarbonate capsule that was then located inside a plastic straw attached to the MPMS3 sample rod. Field-cooled (FC) measurements were applied in the temperature ranging from 2 to 300 K under a DC magnetic field of 100 Oe.

https://doi.org/10.1021/acs.inorgchem.2c04433
Inorg. Chem. XXXX, XXX, XXX–XXX

Diamagnetic correction was performed on the collected data using Pascal's constant.[33]

RESULTS AND DISCUSSION

Chemical and Structural Characterization. SEM of as-synthesized $Cs_{10}MnSb_6Cl_{30}$ SCs indicated imperfect transparent hexagons with evidence of twin boundaries at the surface as demonstrated in Figure 2. EDS analyses were performed at nine sites on three single crystals of $Cs_{10}MnSb_6Cl_{30}$, confirming the stoichiometry of the crystals. A few smaller single crystals of different morphologies with a clear phase boundary from the main phase $Cs_{10}MnSb_6Cl_{30}$ were observed, Figure 2d; EDS confirms these as $Cs_3Sb_2Cl_9$, Table 1. It is important to note that these $Cs_3Sb_2Cl_9$ crystals are present in negligible amounts and were only rarely detected due to the different morphologies; the scarcity of these crystals in samples prepared under hydrothermal conditions means that they were undetectable by all other techniques used in this study. Due to the high Sb^{3+} concentration utilized in the hydrothermal reaction, the cocrystallization of both $Cs_3Sb_2Cl_9$ and $Cs_{10}MnSb_6Cl_{30}$ is very difficult to inhibit; however, the former was present in only very small amounts as to be undetectable by XRD. Although an excess of $MgCl_2$ was added to achieve the required chloride ion concentration, no Mg could be detected in the single crystals by EDS. EDS mapping was also performed at four sites on $Cs_{10}MnSb_6Cl_{30}$ powder prepared by solid-state synthesis as demonstrated in Table 1 and Figure S1.

The crystal structure of $Cs_{10}MnSb_6Cl_{30}$ was determined at 173 K by single-crystal X-ray diffraction (SCXRD), Table 2.

Table 2. Selected Crystallographic Data for $Cs_{10}MnSb_6Cl_{30}$

formula	$Cs_{10}MnSb_6Cl_{30}$
formula weight (g/mol)	3178.04
crystal description	colorless plate
crystal size (mm)	0.09 × 0.06 × 0.01
crystal system	orthorhombic
space group	*Pnnm* (no. 58)
a (Å)	30.7287(7)
b (Å)	12.99555(3)
c (Å)	7.5200(3)
volume (Å^3)	2993.75(13)
Z	2
density (calc., g/cm^3)	3.526
absorption coefficient (mm^{-1})	10.213
F(000)	2782
θ range (deg)	1.706−29.752
no. of reflections collected	52 396
no. of unique reflections (R_{int})	8078 (0.0356)
parameters, restraints	129, 0
goodness of fit on F^2	1.015
R_1, wR_2 [$I > 2\sigma(I)$]	0.0297, 0.0825
R_1, wR_2 (all data)	0.0409, 0.0863
largest difference peak/hole [e/Å^3]	2.438, −0.724

Based on the SCXRD data, $Cs_{10}MnSb_6Cl_{30}$ is found as an orthorhombic phase in the space group *Pnnm* (space group #58). Additional data collections were also undertaken at room temperature and 100 K, both of which showed isostructural unit cells. Phase purity and lattice parameters of samples prepared by the various routes were also confirmed by powder X-ray diffraction (PXRD), Figures 3 and S2. Initial PXRD data from crushed single crystals of $Cs_{10}MnSb_6Cl_{30}$ showed systematic intensity variations associated with preferred orientation, and Rietveld refinements were performed after regrinding the single crystals into finer particles. To correlate the preferred orientation in ground single crystals, spherical harmonic functions were employed to refine the texture in the sample as shown in Figure 3a.[34] The increased intensity of (*h*00)-indexed peaks indicates that the PXRD pattern obtained from ground SCs exhibits crystallographic preferred orientation along the closed-packing (100) direction and is consistent with the plate-like hexagonal-shaped single crystals obtained. There was no evidence of preferred orientation in either the solid-state synthesized $Cs_{10}MnSb_6Cl_{30}$ sample or solution-prepared $Cs_4MnSb_2Cl_{12}$. All $Cs_{10}MnSb_6Cl_{30}$ samples appear single phase despite the observation of $Cs_3Sb_2Cl_9$ single crystals during SEM and EDS analyses; this confirms that this secondary phase is present in only very small amounts as to be undetectable by XRD. The refinements of both solid-state and crushed SC $Cs_{10}MnSb_6Cl_{30}$ samples yield similar lattice parameters.

From the TGA analysis, it can be observed that $Cs_{10}MnSb_6Cl_{30}$ is thermally stable until 545 K in an inert atmosphere as demonstrated in Figure S5a. From DSC analysis and dielectric spectroscopy data shown in Figures S4 and S5b, there is no evidence of any phase transitions between 50 and 545 K.

As illustrated in Figure 4, $Cs_{10}MnSb_6Cl_{30}$ is a 10H perovskite with $(hcccc)_2$ stacking but with ordered vacancies in both FSO and CSO octahedral sites. Initially ignoring the vacancies for clarity, the 10H structure can be described by a successive stacking of FSO layers separated by CSO blocks three octahedra deep. The Mn cations selectively occupy only the middle CSO layer within these blocks. Hence, a complete sequence can be viewed as the succession of three CSO blocks and two FSO blocks. An important feature is the vacancy distribution among the five octahedral layers, which leads to a dimensionality reduction from 3D to 1D. Four crystallographic octahedral sites are labeled in Figure 4, where Sb(01) and Sb(02) fully occupy the outer layers of the CSO block and Sb(03) is distributed in an ordered fashion across 50% of the octahedral sites in the FSO block. This distribution results in a distorted "checkerboard" ordering within each layer but with an offset between the layers such that there are no face-sharing Sb_2Cl_9 dimers. The Mn^{2+}, located in the middle CSO layer, also occupies 50% of the octahedral sites in this layer in a similar checkerboard ordered fashion. From Figure 4, it can be observed that the vacancy ordering in $Cs_{10}MnSb_6Cl_{30}$ can be described by a combination of checkerboard ordering of vacancies in both the half-occupied FSO and Mn-containing CSO layers, and which disrupt the connectivity, resulting in 1D $[MnSb_6Cl_{30}]^{10-}{}_n$ columns running along the *c*-axis of the *Pnnm* structure (*i.e.*, orthogonal to the AX_3 stacking direction).

Vacancy-ordered structures appear to be energetically favorable during aliovalent doping for both close-packed hexagonal halide and oxide perovskites.[16,35,36] In $A_3B_2X_9$ halides, the preferred vacant octahedral site is mainly determined by the relative ionic size and electron configuration of B^{3+}. For example, in β-$Cs_3Sb_2Cl_9$,[37] vacancies tend to occupy the FSO to form a similar "checkerboard" distribution as in $Cs_{10}MnSb_6Cl_{30}$. This is to avoid B−B repulsion in FSO dimers due to the close distance (about 2.943 Å) between two hexagonal packed $SbCl_6$ and the poor screening due to the relatively low polarizability of the chloride ion, resulting in the

https://doi.org/10.1021/acs.inorgchem.2c04433
Inorg. Chem. XXXX, XXX, XXX−XXX

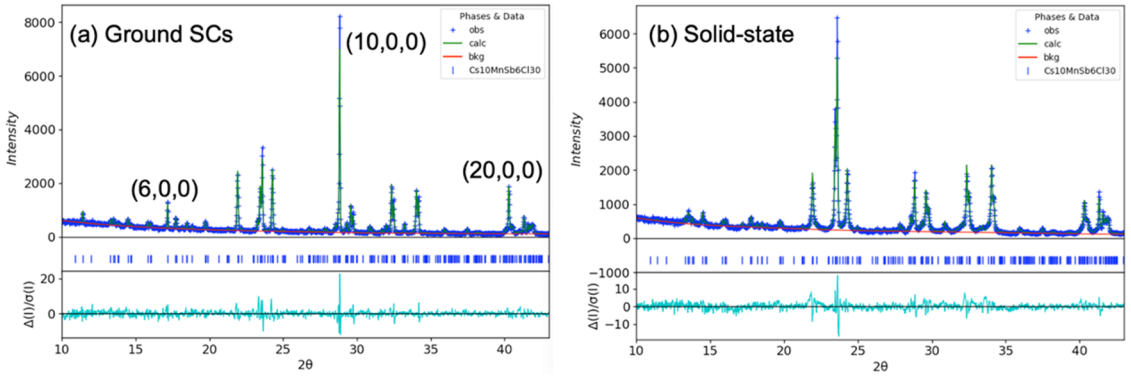

Figure 3. Rietveld refinement profiles for powder X-ray diffraction data of (a) ground single crystals of $Cs_{10}MnSb_6Cl_{30}$ and (b) solid-state synthesized $Cs_{10}MnSb_6Cl_{30}$, confirming the formation of 10H phase as determined from single-crystal XRD.

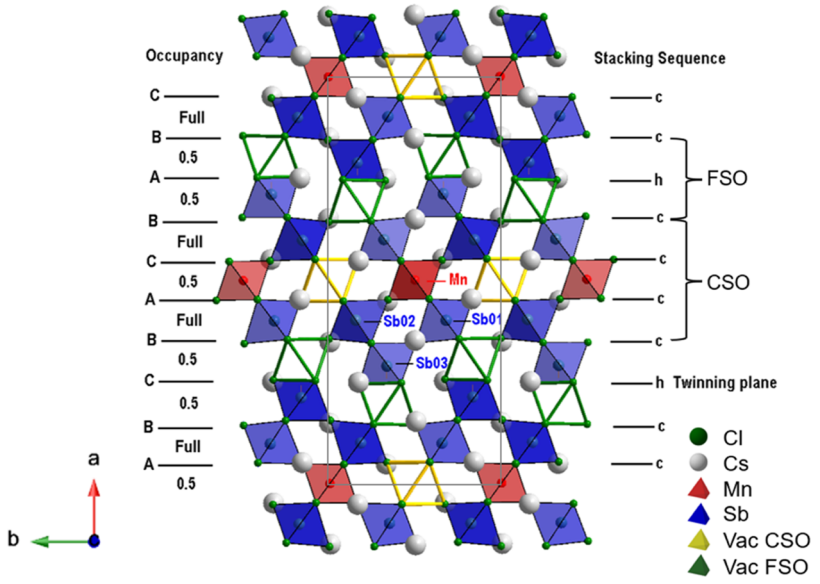

Figure 4. Structure of the vacancy-ordered $(hcccc)_2$ type 10H layered $Cs_{10}MnSb_6Cl_{30}$ perovskite viewed along the *c*-axis (in the packing layer plane). To emphasize the underlying 10H parent structure, vacant polyhedra are outlined, with occupied polyhedra shown as shaded.

formation of a 1D 6H $(hcc)_2$ structure.[38] However, in $Cs_3Sb_2I_9$, vacancies prefer to occupy the CSO sequence because of the relatively larger distance (ca. 3.97 Å) and weaker influence of lone pair electrons between two hexagonal packed layers and better screening provided by I^-, hence yielding a 0D 6H $(hcc)_2$ structure. If a cation smaller than Sb is incorporated, such as $Cs_3Cr_2Cl_9$,[39] a preferred distribution of vacancies at CSO sites is observed. In comparison with deficient halides, vacancies in analogous B-site-deficient oxides normally preferentially appear in the FSO. For instance, in the similar deficient 10H $(hcccc)_2$ $Ba_{10}Mg_{0.25}Ta_{7.9}O_{30}$, the long-range ordering of vacancies at FSO blocks was determined by TEM, although the periodicity of the ordered vacancies is more complex than the zig-zag chains of $Cs_{10}MnSb_6Cl_{30}$ and results in retention of 3D octahedral connectivity.[40] Compared to 10H oxide analogues with only FSO vacancies, the 10H halide $Cs_{10}MnSb_6Cl_{30}$ contains a higher vacancy ratio of 3/10 with both FSO and CSO vacancies, resulting in a further loss of connectivity to form a 1D structure. Such coexistence of both CSO and FSO vacancies to form isolated 1D columns is rarely observed in either oxide or halide perovskites.

Magnetic Properties. To investigate any magnetic coupling between Mn^{2+} in $Cs_{10}MnSb_6Cl_{30}$, magnetic susceptibility was collected in the temperature range 2−300 K. Despite some noise in the data, presumably due to the low field used and possibly due to some settling of the plate-like single crystals used in the measurement, a linear fitting from 40 to 300 K using the Curie−Weiss law, Figure 5, yields a Weiss constant of −9.43(8) K and an effective magnetic moment of 5.494(5) μ_B. Although a little low due to data quality as mentioned above, the magnitude of the moment is consistent

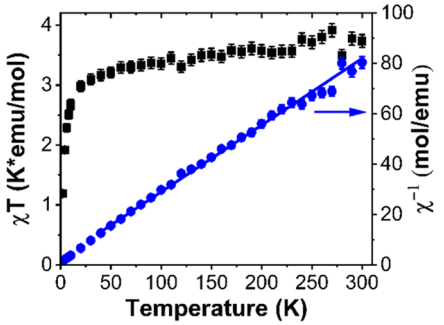

Figure 5. Temperature dependence of magnetic properties for $Cs_{10}MnSb_6Cl_{30}$.

https://doi.org/10.1021/acs.inorgchem.2c04433
Inorg. Chem. XXXX, XXX, XXX−XXX

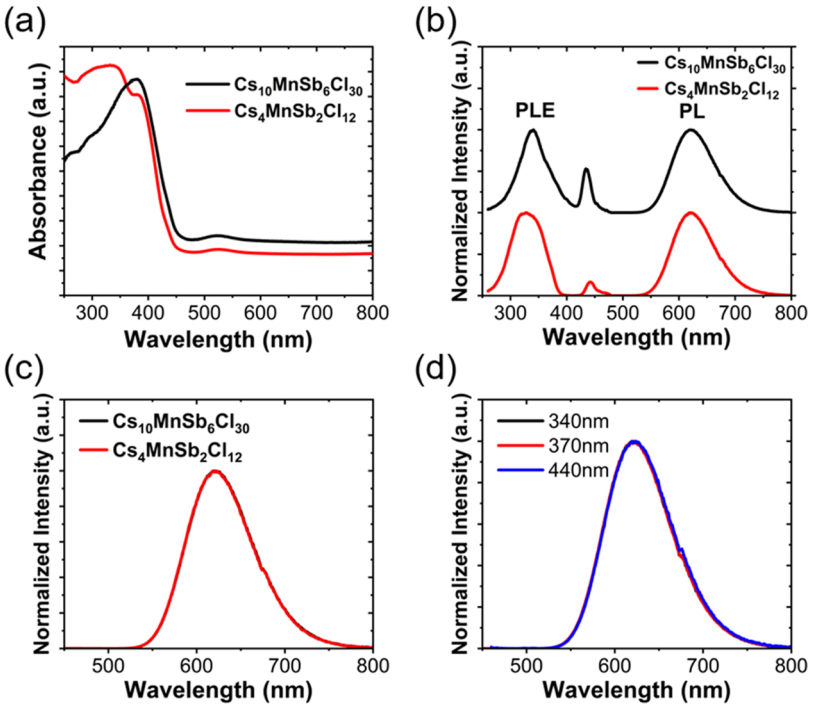

Figure 6. (a) Steady-state absorbance spectra for $Cs_4MnSb_2Cl_{12}$ and $Cs_{10}MnSb_6Cl_{30}$; (b) steady-state PL (excited at 340 nm) and PLE (detected at 620 nm) spectra for $Cs_4MnSb_2Cl_{12}$ and $Cs_{10}MnSb_6Cl_{30}$ (note the data are offset on the *y*-axis for clarity); (c) PL spectra excited at 340 nm for $Cs_4MnSb_2Cl_{12}$ and $Cs_{10}MnSb_6Cl_{30}$; and (d) PL spectra of $Cs_{10}MnSb_6Cl_{30}$ for excitation at 340, 370, and 440 nm.

with the theoretical value 5.916 μ_B for spin-only moment of high spin state d^5 Mn^{2+} and further corroborates the inclusion of Mn^{2+}. The negative Weiss constant indicates weak antiferromagnetic coupling between Mn^{2+}. Such weak super-exchange was also predicted and observed in both 2D $Cs_4MnSb_2Cl_{12}$ and $Cs_4MnBi_2Cl_{12}$, which is attributed to the four bond Mn−Cl−(Sb/Bi)−Cl−Mn exchange pathway.[27,41] The product of magnetic susceptibility and temperature is only slowly varying over most of the high temperature range, further supporting the existence of weak antiferromagnetic interactions and a constant effective moment per site.

Optical Properties. UV−vis diffuse reflectance of $Cs_{10}MnSb_6Cl_{30}$ was measured and converted into pseudoabsorbance using the Kubelka−Munk (KM) transformation $\alpha = (1 - R)^2/2R$, where α is the absorption coefficient and R is the reflectance.[32] Equivalent data for $Cs_4MnSb_2Cl_{12}$ were collected to allow comparison and are shown in Figure 6a. The spectra demonstrate that $Cs_{10}MnSb_6Cl_{30}$ shows similar behavior to $Cs_4MnSb_2Cl_{12}$ with the main absorption onset at around 450 nm. Both compounds exhibit weak absorption at about 520 nm, which is assigned to the forbidden $^6A_1(S) \rightarrow {}^4T_1(G)$ d−d transition of high spin Mn^{2+}.[41,42] For $Cs_4MnSb_2Cl_{12}$, two additional strong absorption peaks are observed at ca. 350 and 380 nm and are ascribed to the partially allowed $^1S_0 \rightarrow {}^3P_1$ transition of Sb^{3+} split by a second-order Jahn−Teller distortion.[43−45] In comparison with the 3C $Cs_4MnSb_2Cl_{12}$ polytype, only one strong, well-defined absorption peak is observed at 380 nm for $Cs_{10}MnSb_6Cl_{30}$, which is also likely due to the $^1S_0 \rightarrow {}^3P_1$ transition of Sb^{3+}. Tauc plots of $Cs_{10}MnSb_6Cl_{30}$ were obtained assuming both a direct and indirect band gap, giving values of 2.98 and 2.69 eV, respectively (see the Supporting Information for further details). While indirect band gaps are typically expected for perovskites with adjacent occupied FSO, the combination of the checkerboard ordering in-plane and the zig-zag arrangement between FSO results in no Sb−Sb FSO in this case, and so, the electronic structure is likely to be dominated by CSO orbital interactions. To verify this, DFT calculations need to be performed; these are underway but are complex and time-consuming due to the heavy ions involved and also large supercell volumes associated with the various permutations of the antiferromagnetically ordered ground state. However, considering the structural and compositional similarity to $Cs_4MnSb_2Cl_{12}$, which also has no 90° Sb−Cl−Sb interactions, a 2.98 eV direct band gap may be tentatively assumed for $Cs_{10}MnSb_6Cl_{30}$.

Steady-state photoluminescence emission (PL), photoluminescence excitation (PLE), and photoluminescence quantum yield (PLQY) data were collected from both $Cs_4MnSb_2Cl_{12}$ and $Cs_{10}MnSb_6Cl_{30}$ powders at room temperature. The PL spectra show wide peaks centered at 620 nm with a full width at half-maximum (FWHM) of ca. 88 nm as illustrated in Figure 6b,c, indicating that the same PL mechanism attributed to the octahedrally coordinated Mn^{2+} transition from $^4T_1$ to $^6A_1$ for both $Cs_{10}MnSb_6Cl_{30}$ and the previously reported $Cs_4MnSb_2Cl_{12}$.[27] In addition to a peak at 340 nm (which we attribute to the onset of $^1S_0 \rightarrow {}^3P_1$ transition of Sb^{3+}), the PLE data of $Cs_{10}MnSb_6Cl_{30}$ show a strong peak at 440 nm, which corresponds to the $^6A_1(S) \rightarrow {}^4T_2(G)$ transitions of high spin Mn^{2+}.[45] However, the emission is independent of excitation wavelength (Figure 6d), indicating that the same species is likely to be responsible for the emission under excitation wavelengths from 340 to 440 nm. In $Cs_4MnSb_2Cl_{12}$, the 440 nm feature in PLE is smaller and the emission spectrum is the same for all excitation wavelengths (Figures 6b and S8). The $Cs_{10}MnSb_6Cl_{30}$ samples exhibit larger PLQYs than $Cs_4MnSb_2Cl_{12}$. The PLQY of $Cs_{10}MnSb_6Cl_{30}$ was 3.5±1% for excitation at 340 nm and

https://doi.org/10.1021/acs.inorgchem.2c04433
Inorg. Chem. XXXX, XXX, XXX−XXX

12.5 ± 1% for excitation at 440 nm (Table 3). For $Cs_4MnSb_2Cl_{12}$, the PLQY was 1.3 ± 1% for both excitation

Table 3. Average Quantum Yield Excited at 340 and 440 nm

	average PLQY (%)	
excitation wavelength (nm)	340 nm	440 nm
$Cs_4MnSb_2Cl_{12}$	1.3 ± 1	1.3 ± 1
$Cs_{10}MnSb_6Cl_{30}$	3.5 ± 1	12.5 ± 1

wavelengths. The higher PLE and PLQY of $Cs_{10}MnSb_6Cl_{30}$ may suggest that the forbidden d−d transition ($^4T_1$ to $^6A_1$) may be increasingly allowed due to a symmetry reduction of the $MnCl_6$ octahedra as a result of a local distortion; however, further experiments are required to clarify this and, in particular, the reason for the higher PLQY under 440 nm excitation.

CONCLUSIONS

In conclusion, a novel one-dimensional perovskite $Cs_{10}MnSb_6Cl_{30}$ with a unique vacancy-ordered 10H structure has been prepared and is the first reported 10H halide perovskite. In comparison to the vacancy-ordered 3C $Cs_4MnSb_2Cl_{12}$ phase, which displays 2D (layered) octahedral connectivity, the specific vacancy ordering in the 10H $Cs_{10}MnSb_6Cl_{30}$ compound further reduces this dimensionality to 1D (columnar). As a result, the 10H-type $Cs_{10}MnSb_6Cl_{30}$ exhibits stronger photoluminescence and improved PLQY compared to the reported 3C-type $Cs_4MnSb_2Cl_{12}$. The current study highlights structural tuning via vacancy ordering as a mechanism to obtain low-dimensional halide perovskites with enhanced optical properties.

ASSOCIATED CONTENT

Data Availability Statement

The research data underpinning this publication can be accessed at https://doi.org/10.17630/51767b58-94a9-4ab2-9f93-c4c7edc4fdd0 [ref 46].

Supporting Information

The Supporting Information is available free of charge at https://pubs.acs.org/doi/10.1021/acs.inorgchem.2c04433.

Materials characterization methods and data including compositional analysis; single-crystal and powder X-ray diffraction; UV−VIS, TGA−DCS, and dielectric data; photoluminescence and quantum yield data (PDF)

Accession Codes

CCDC 2194265 contains the supplementary crystallographic data for this paper. These data can be obtained free of charge via www.ccdc.cam.ac.uk/data_request/cif, or by emailing data_request@ccdc.cam.ac.uk, or by contacting The Cambridge Crystallographic Data Centre, 12 Union Road, Cambridge CB2 1EZ, UK; fax: +44 1223 336033.

AUTHOR INFORMATION

Corresponding Author

Finlay D. Morrison − *EaStCHEM School of Chemistry, University of St. Andrews, St. Andrews KY16 9ST, U.K.;* orcid.org/0000-0002-2813-3142; Email: finlay.morrison@st-andrews.ac.uk

Authors

Hang Liu − *EaStCHEM School of Chemistry, University of St. Andrews, St. Andrews KY16 9ST, U.K.*

Hassan Hafeez − *Organic Semiconductor Centre, School of Physics and Astronomy, SUPA, University of St. Andrews, St. Andrews KY16 9SS, U.K.*

David B. Cordes − *EaStCHEM School of Chemistry, University of St. Andrews, St. Andrews KY16 9ST, U.K.;* orcid.org/0000-0002-5366-9168

Alexandra M. Z. Slawin − *EaStCHEM School of Chemistry, University of St. Andrews, St. Andrews KY16 9ST, U.K.;* orcid.org/0000-0002-9527-6418

Gavin Peters − *EaStCHEM School of Chemistry, University of St. Andrews, St. Andrews KY16 9ST, U.K.*

Stephen L. Lee − *School of Physics and Astronomy, SUPA, University of St. Andrews, St. Andrews KY16 9SS, U.K.*

Ifor D. W. Samuel − *Organic Semiconductor Centre, School of Physics and Astronomy, SUPA, University of St. Andrews, St. Andrews KY16 9SS, U.K.;* orcid.org/0000-0001-7821-7208

Complete contact information is available at: https://pubs.acs.org/10.1021/acs.inorgchem.2c04433

Notes

The authors declare no competing financial interest.

ACKNOWLEDGMENTS

H.L. would like to thank the University of St. Andrews for financial support via a St. Leonard's scholarship. The authors acknowledge facilities access made possible through support from the EPSRC Light Element Analysis facility Grant EP/T019298/1 and the EPSRC Strategic Equipment Resource Grant EP/R023751/1.

REFERENCES

(1) Saparov, B.; Mitzi, D. B. Organic-Inorganic Perovskites: Structural Versatility for Functional Materials Design. *Chem. Rev.* **2016**, *116*, 4558−96.

(2) Megaw, H. D. Crystal Structure of Double Oxides of the Perovskite Type. *Proc. Phys. Soc.* **1946**, *58*, 133−152.

(3) Szafrański, M.; Katrusiak, A.; Ståhl, K. Time-dependent transformation routes of perovskites $CsPbBr_3$ and $CsPbCl_3$ under high pressure. *J. Mater. Chem. A* **2021**, *9*, 10769−10779.

(4) Takeda, Y.; Kanamura, F.; Shimada, M.; Koizumi, M. The crystal structure of $BaNiO_3$. *Acta Crystallogr., Sect. B: Struct. Sci. Cryst. Eng. Mater.* **1976**, *32*, 2464−2466.

(5) Raw, A. D.; Ibers, J. A.; Poeppelmeier, K. R. Syntheses and structure of hydrothermally prepared $CsNiX_3$ (X=Cl, Br, I). *J. Solid State Chem.* **2012**, *192*, 34−37.

(6) Nguyen, L. T.; Cava, R. J. Hexagonal Perovskites as Quantum Materials. *Chem. Rev.* **2021**, *121*, 2935−2965.

(7) Stein, F.; Palm, M.; Sauthoff, G. Structure and stability of Laves phases. Part I. Critical assessment of factors controlling Laves phase stability. *Intermetallics* **2004**, *12*, 713−720.

(8) Culbertson, C. M.; Flak, A. T.; Yatskin, M.; Cheong, P. H.; Cann, D. P.; Dolgos, M. R. Neutron Total Scattering Studies of Group II Titanates ($ATiO_3$, A(2+) = Mg, Ca, Sr, Ba). *Sci. Rep.* **2020**, *10*, No. 3729.

(9) Usman, M.; Ayer, G. B.; Smith, M. D.; Loye, H.-C. Synthesis and Crystal Structure of a 6H Hexagonal Fluoro-Perovskite: $RbMgF_3$. *J. Chem. Crystallogr.* **2021**, *51*, 9−13.

(10) de Muro, I. G.; Insausti, M.; Lezama, L.; Rojo, T. Effect of the synthesis conditions on the magnetic and electrical properties of the $BaFeO_{3-x}$ oxide: A metamagnetic behavior. *J. Solid State Chem.* **2005**, *178*, 1712−1719.

(11) Kuang, X.; Allix, M. M. B.; Claridge, J. B.; Niu, H. J.; Rosseinsky, M. J.; Ibberson, R. M.; Iddles, D. M. Crystal structure, microwave dielectric properties and AC conductivity of B-cation deficient hexagonal perovskites $La_5MxTi_{4-x}O_{15}$ (x = 0.5, 1; M = Zn, Mg, Ga, Al). *J. Mater. Chem.* **2006**, *16*, 1038.
(12) Yin, C.; Tian, G.; Li, G.; Liao, F.; Lin, J. New 10H perovskites $Ba_5Ln_{1-x}Mn_{4+y}O_{15-\delta}$ with spin glass behaviour. *RSC Adv.* **2017**, *7*, 33869−33874.
(13) Cao, W.; Yang, X.; Lu, F.; Zhu, W.; Liu, L.; Kuang, X.; Allix, M. 8H-10H Stacking Periodicity Control in Twinned Hexagonal Perovskite Dielectrics. *Inorg. Chem.* **2018**, *57*, 4117−4124.
(14) Tian, J.; Cordes, D. B.; Slawin, A. M. Z.; Zysman-Colman, E.; Morrison, F. D. Progressive Polytypism and Bandgap Tuning in Azetidinium Lead Halide Perovskites. *Inorg. Chem.* **2021**, *60*, 12247−12254.
(15) Kamminga, M. E.; de Wijs, G. A.; Havenith, R. W. A.; Blake, G. R.; Palstra, T. T. M. The Role of Connectivity on Electronic Properties of Lead Iodide Perovskite-Derived Compounds. *Inorg. Chem.* **2017**, *56*, 8408−8414.
(16) Han, Y.; Yue, S.; Cui, B. B. Low-Dimensional Metal Halide Perovskite Crystal Materials: Structure Strategies and Luminescence Applications. *Adv. Sci.* **2021**, *8*, No. 2004805.
(17) Kim, E.-B.; Akhtar, M. S.; Shin, H.-S.; Ameen, S.; Nazeeruddin, M. K. A review on two-dimensional (2D) and 2D-3D multidimensional perovskite solar cells: Perovskites structures, stability, and photovoltaic performances. *J. Photochem. Photobiol. C* **2021**, *48*, No. 100405.
(18) Lehner, A. J.; Fabini, D. H.; Evans, H. A.; Hébert, C.-A.; Smock, S. R.; Hu, J.; Wang, H.; Zwanziger, J. W.; Chabinyc, M. L.; Seshadri, R. Crystal and Electronic Structures of Complex Bismuth Iodides $A_3Bi_2I_9$ (A = K, Rb, Cs) Related to Perovskite: Aiding the Rational Design of Photovoltaics. *Chem. Mater.* **2015**, *27*, 7137−7148.
(19) Pradhan, A.; Sahoo, S. C.; Sahu, A. K.; Samal, S. L. Effect of Bi Substitution on $Cs_3Sb_2Cl_9$: Structural Phase Transition and Band Gap Engineering. *Cryst. Growth Des.* **2020**, *20*, 3386−3395.
(20) Morgan, E. E.; Mao, L.; Teicher, S. M. L.; Wu, G.; Seshadri, R. Tunable Perovskite-Derived Bismuth Halides: $Cs_3Bi_2(Cl_{1-x}I_x)_9$. *Inorg. Chem.* **2020**, *59*, 3387−3393.
(21) Pramod, A. K.; Raj Subramaniam, M.; Hevia, S. A.; Batabyal, S. K. Synthesis of lead-free $Cs_3Sb_2Cl_3Br_6$ halide perovskite through solution processing method for self-powered photodetector applications. *Mater. Lett.* **2022**, *306*, No. 130874.
(22) Hoard, J. L.; Goldstein, L. The Crystal Structure of Cesium Enneachlordithalliate, $Cs_3Tl_2Cl_9$. *J. Chem. Phys.* **1935**, *3*, 199−202.
(23) Liu, C.; Wang, Y.; Geng, H.; Zhu, T.; Ertekin, E.; Gosztola, D.; Yang, S.; Huang, J.; Yang, B.; Han, K.; Canton, S. E.; Kong, Q.; Zheng, K.; Zhang, X. Asynchronous Photoexcited Electronic and Structural Relaxation in Lead-Free Perovskites. *J. Am. Chem. Soc.* **2019**, *141*, 13074−13080.
(24) Chabot, B.; Parthe, E. $Cs_3Sb_2I_9$ and $Cs_3Bi_2I_9$ with the hexagonal $Cs_3Cr_2Cl_9$ structure type. *Acta Crystallogr., Sect. B: Struct. Sci. Cryst. Eng. Mater.* **1978**, *34*, 645−648.
(25) Tailor, N. K.; Satapathi, S. Photosensitive Dielectric and Conductivity Relaxation in Lead-Free $Cs_3Bi_2Cl_9$ Perovskite Single Crystals. *J. Phys. Chem. C* **2021**, *125*, 5243−5250.
(26) Gray, M. B.; Majher, J. D.; Holzapfel, N. P.; Woodward, P. M. Exploring the Stability of Mixed-Halide Vacancy-Ordered Quadruple Perovskites. *Chem. Mater.* **2021**, *33*, 2165−2172.
(27) Vargas, B.; Torres-Cadena, R.; Rodríguez-Hernández, J.; Gembicky, M.; Xie, H.; Jiménez-Mier, J.; Liu, Y.-S.; Menéndez-Proupin, E.; Dunbar, K. R.; Lopez, N.; Olalde-Velasco, P.; Solis-Ibarra, D. Optical, Electronic, and Magnetic Engineering of ⟨111⟩ Layered Halide Perovskites. *Chem. Mater.* **2018**, *30*, 5315−5321.
(28) Arramel; Maddalena, F.; Mahyuddin, M. H.; Yin, X.; Tang, C. S.; Agusta, M. K.; Sahdan, M. F.; Diao, C.; Dang, C.; Birowosuto, M. D.; Wee, A. T. S.; Rusydi, A. Temperature-induced orbital polarizations and tunable charge dynamics in layered double perovskite thin films. *Mater. Today Energy* **2022**, *24*, No. 100921.
(29) He, S.; Fang, S.; Han, T.; Lang, T.; Cai, M.; You, H.; Peng, L.; Cao, S.; Liu, B.; Qiang, Q.; Chen, J.; Lei, B. Spectral Red Shift of $Cs_4Mn(Bi_{1-x}In_x)_2Cl_{12}$ Layered Double Perovskite by Adjusting the Microstructure of the $[MnCl_6]^{4-}$ Octahedron. *J. Phys. Chem. C* **2021**, *125*, 16938−16945.
(30) Vargas, B.; Torres-Cadena, R.; Reyes-Castillo, D. T.; Rodríguez-Hernández, J.; Gembicky, M.; Menéndez-Proupin, E.; Solis-Ibarra, D. Chemical Diversity in Lead-Free, Layered Double Perovskites: A Combined Experimental and Computational Approach. *Chem. Mater.* **2020**, *32*, 424−429.
(31) Toby, B. H.; Von Dreele, R. B. GSAS-II: the genesis of a modern open-source all purpose crystallography software package. *J. Appl. Crystallogr.* **2013**, *46*, 544−549.
(32) Makuła, P.; Pacia, M.; Macyk, W. How To Correctly Determine the Band Gap Energy of Modified Semiconductor Photocatalysts Based on UV-Vis Spectra. *J. Phys. Chem. Lett.* **2018**, *9*, 6814−6817.
(33) Bain, G. A.; Berry, J. F. Diamagnetic corrections and Pascal's constants. *J. Chem. Educ.* **2008**, *85*, 532.
(34) Bergmann, J.; Monecke, T.; Kleeberg, R. Alternative algorithm for the correction of preferred orientation in Rietveld analysis. *J. Appl. Crystallogr.* **2001**, *34*, 16−19.
(35) Tao, F.; Genevois, C.; Lu, F.; Kuang, X.; Porcher, F.; Li, L.; Yang, T.; Li, W.; Zhou, D.; Allix, M. First 14-Layer Twinned Hexagonal Perovskite $Ba_{14}Mn_{1.75}Ta_{10.5}O_{42}$: Atomic-Scale Imaging of Cation Ordering. *Chem. Mater.* **2016**, *28*, 4686−4696.
(36) Kim, S. W.; Zhang, R.; Halasyamani, P. S.; Hayward, M. A. $K_4Fe_3F_{12}$: An Fe(2+)/Fe(3+) Charge-Ordered, Ferrimagnetic Fluoride with a Cation-Deficient, Layered Perovskite Structure. *Inorg. Chem.* **2015**, *54*, 6647−52.
(37) Kihara, K.; Sudo, T. The crystal structures of β-$Cs_3Sb_2Cl_9$ and $Cs_3Bi_2Cl_9$. *Acta Crystallogr., Sect. B: Struct. Sci. Cryst. Eng. Mater.* **1974**, *30*, 1088−1093.
(38) Madden, P. A.; Wilson, M. 'Covalent' effects in 'ionic'systems. *Chem. Soc. Rev.* **1996**, *25*, 339−350.
(39) Saßmannshausen, M.; Lutz, H. Caesiumchromhalogenide Cs_3CrCl_6, $Cs_3Cr_2Cl_9$ und Cs_3CrBr_6−Darstellung, Eigenschaften, Kristallstruktur. *Z. Anorg. Allgem. Chem.* **2001**, *627*, 1071−1076.
(40) Mallinson, P.; Claridge, J.; Iddles, D.; Price, T.; Ibberson, R.; Allix, M.; Rosseinsky, M. New 10-layer hexagonal perovskites: relationship between cation and vacancy ordering and microwave dielectric loss. *Chem. Mater.* **2006**, *18*, 6227−6238.
(41) Holzapfel, N. P.; Majher, J. D.; Strom, T. A.; Moore, C. E.; Woodward, P. M. $Cs_4Cd_{1-x}Mn_xBi_2Cl_{12}$—A Vacancy-Ordered Halide Perovskite Phosphor with High-Efficiency Orange-Red Emission. *Chem. Mater.* **2020**, *32*, 3510−3516.
(42) Mehra, A. Optical Absorption of Mn2+-Doped Alkali Halides. *Phys. Status Solidi B* **1968**, *29*, 847−857.
(43) Sartori, E.; Campolucci, M.; Baranov, D.; Zeng, M.; Toso, S.; Divitini, G.; Ferretti, M.; Hens, Z.; Manna, L.; Locardi, F. Red-emissive nanocrystals of $Cs_4Mn_xCd_{1-x}Sb_2Cl_{12}$ layered perovskites. *Nanoscale* **2022**, *14*, 305−311.
(44) Noculak, A.; Morad, V.; McCall, K. M.; Yakunin, S.; Shynkarenko, Y.; Worle, M.; Kovalenko, M. V. Bright Blue and Green Luminescence of Sb(III) in Double Perovskite Cs_2MInCl_6 (M = Na, K) Matrices. *Chem. Mater.* **2020**, *32*, 5118−5124.
(45) Vargas, B.; Coutino-Gonzalez, E.; Ovalle-Encinia, O.; Sanchez-Ake, C.; Solis-Ibarra, D. Efficient Emission in Halide Layered Double Perovskites: The Role of Sb(3+) Substitution in $Cs_4Cd_{1-x}Mn_xBi_2Cl_{12}$ Phosphors. *J. Phys. Chem. Lett.* **2020**, *11*, 10362−10367.
(46) Liu, H.; Hafeez, H.; Cordes, D. B.; Slawin, A. M. Z.; Peters, G.; Lee, S.; Samuel, I. D. W.; Morrison, F. D. Enhanced Photoluminescence and Reduced Dimensionality Via Vacancy Ordering in a 10H Halide Perovskite (Dataset) University of St Andrews Research Portal 2023 DOI: 10.17630/51767b58-94a9-4ab2-9f93-c4c7edc4fdd0.

https://doi.org/10.1021/acs.inorgchem.2c04433
Inorg. Chem. XXXX, XXX, XXX−XXX